Unbalanced Axial Forces in Axial-Flux Machines

Wen L. Soong
School of Electrical Engineering
University of Adelaide
Adelaide, Australia
wen.soong@adelaide.edu.au

Zhi Cao, Emad Roshandel,
Amin Mahmoudi
College of Science & Engineering
Flinders University
Adelaide, Australia
zhi.cao@flinders.edu.au
emad.roshandel@flinders.edu.au
amin.mahmoudi@flinders.edu.au

Solmaz Kahourzade
STEM
University of South Australia
Adelaide, Australia
solmaz.kahourzade@unisa.edu.au

***Abstract*—This paper performs an analysis of the variation of unbalanced forces with airgap length in axial-flux machines. A simple analytical approach is used to provide insights into these key parameters and the results compared with finite-element results for both axial-flux permanent magnet (PM) and induction machines. For PM and current-driven induction machines, the two most important parameters are the ratio of the effective magnet/core magnetic path length to the nominal airgap, and the ratio of the saturation flux density to the nominal airgap flux density. For voltage-driven induction machines, the key parameter is the ratio of stator leakage inductance to the nominal magnetising inductance.**

***Index Terms*—axial-flux machines, axial force, finite-element analysis, negative stiffness, saturation, unbalanced force**

I. Introduction

Unbalanced forces can occur both in radial- and axial-flux electric machines. For radial-flux machines, the radial forces on the rotor are balanced, and unbalanced radial forces are only produced by airgap eccentricity, see Fig. 1. On the other hand, axial-flux machines with only a single stator and rotor will inherently have a significant unbalanced axial force between them.

More challenging than just the large axial force is that there can be a large increase in this force with a small reduction in axial airgap length. This effectively produces a high negative stiffness. While using multiple stators and/or rotors in double-sided axial flux machines can be used to eliminate the unbalanced force at the nominal airgap, this does not necessarily eliminate the negative stiffness, which can be up to double in magnitude in such machines compared to single-sided machines. To reduce the negative stiffness in double-sided machines, it is necessary that the magnetic flux path in the machines crosses both airgaps.

Axial-flux machines have some similarities to axial magnetic bearings, especially in their negative stiffness effects. In axial magnetic bearings, the axial forces are controlled by the stator voltage/currents and their inherent negative stiffness subtracts from the positive stiffness generated by controlling the magnetic bearing coil current as a function of the axial position. Stable operation is achieved when the net stiffness of the system is positive and hence the bearing generates restoring forces in the case of position disturbances.

The financial support of an Australian Research Council grant DP170103343 is gratefully acknowledged.

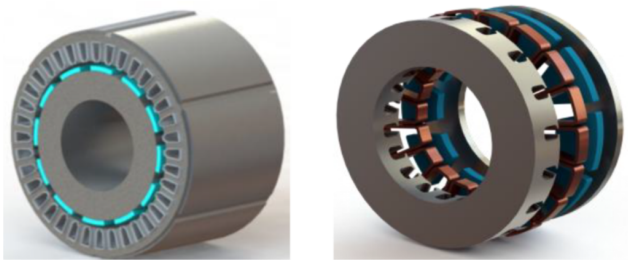

Fig. 1. Radial (left) and axial-flux (right) PM electric machines [1]

In axial-flux machines there is generally no attempt to control the axial forces during machine operation. Thus, careful mechanical design is required to ensure the total positive stiffness of the stator, rotor and bearings exceeds the large inherent negative stiffness of the machine. Otherwise this can result in an undesirable mechanical contact between the stator and rotor.

The authors recently built a prototype axial-flux induction machine and found when the stator voltage was applied, that the axial forces caused the stator and rotor to contact. This incident inspired this paper to investigate these effects in more detail.

This paper uses simplified magnetic and electrical equivalent-circuit models to seek to better understand the variation of axial force with airgap for axial-flux permanent magnet (PM) machines and induction machines (IM).

A. Literature Review

While axial-flux machines have not received as much attention as radial-flux machines, there has been a steady series of papers on this topic over the years. A significant challenge with axial-flux machines is that they are inherently a three-dimensional (3D) machine and hence generally require 3D finite-element analysis (FEA) to obtain higher accuracy. This is unlike radial flux machines where two-dimensional (2D) FEA can often give reasonable accuracy.

The use of 3D FEA is significantly slower than 2D FEA and so when analysing axial-flux machines a number of researchers have used analytical models such as [2]–[5]. These detailed analytical models often model the 3D magnetic field patterns and can include stator slotting and end-effects [2] but generally neglect saturation. To include saturation effects and to obtain higher accuracy results, some researchers have used magnetic equivalent-circuit models [6], [7] while others have used 2D or 3D FEA [6], [8].

Most of the work on axial-flux machine modelling has been focussed on axial-flux PM machines [2]–[9] but there has been some work on axial-flux IMs [10] which modelled the effect of static eccentricity on leakage and magnetising inductances.

This paper seeks to use simplified magnetic circuit and electrical equivalent circuit models to obtain a fundamental understanding of the relationship between axial force versus airgap length for a PM machine and current and voltage-driven axial-flux IMs. While these simplified analytical magnetic circuit models have many assumptions and are much less accurate than the more detailed models in papers such as [2]–[4], they have the advantage of being able to provide improved understanding of the sensitivity of the axial force to the airgap and key normalised design parameters of the machine. It thus shown that for PM/current-excited machines the key parameter is the ratio of the effective magnet and core magnetic path length versus the nominal airgap length, while for voltage-excited induction machines the key parameter is the ratio of leakage to the magnetising reactance at the nominal airgap length. The results are compared with 3D FEA results from an axial-flux PM machine and axial-flux IM.

The layout of this paper is as follows. Section II covers the analytical modelling of the axial force variation for the PM/current-driven and the voltage-driven cases. Section III then presents a case study of an axial-flux PM machine where the analytical and 3D FE results are compared. Similarly Section IV presents a case study of an axial-flux IM for the voltage-driven case. Finally conclusions are drawn in Section V.

II. Axial Force Analysis

Consider the following models of the no-load airgap flux density B_g for the permanent magnet (PM)-excited c-core and the electrically-excited c-core shown in Fig. 2. It is proposed in this work that the PM-excited core can be used to understand the axial force versus airgap for axial-flux PM machines under no-load conditions and that the electrical-excited core can be used to model the axial force versus airgap for axial-flux IMs under both voltage and current excitation. In addition, this model can likely be used for synchronous reluctance machines.

A. Analytical Force Model - PM and Current-Driven Cases

From Fig. 2, using the magnet remanent flux density B_r, the c-core iron core path length l_c, magnet length l_m, airgap length l_g and the relative permeability of the core μ_{rc} and the magnet μ_{rm}, the airgap flux density B_g for the PM-excited core is,

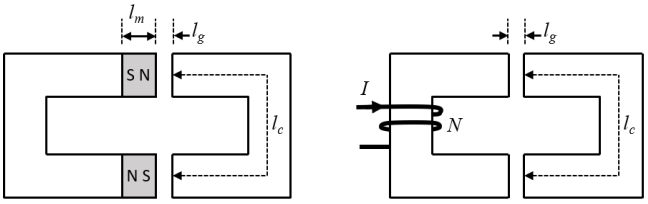

(a) PM-excited (b) Electrically-excited

Fig. 2. Magnetic circuits for the PM- and electrically-excited c-core configurations.

$$B_g(l_g) = B_r \frac{2l_m/\mu_{rm}}{2l_m/\mu_{rm} + 2l_c/\mu_{rc} + 2l_g} \tag{1}$$

while for the electrically-excited core where the mmf NI and the permeability of free space is μ_o, the airgap flux density is,

$$B_g(l_g) = \frac{\mu_0 NI}{2l_c/\mu_{rc} + 2l_g} \tag{2}$$

This analysis neglects fringing effects and slotting effects, and assumes a magnet pole arc of 180°.

The airgap flux density B_g with airgap l_g can be normalised versus the airgap flux density B_{g0} with the nominal airgap l_{g0}. In addition, by defining the effective magnetic magnet and core length $l'_{mc} = l_m/\mu_{rm} + l_c/\mu_{rc}$ in (1) and (2), then for both core types the result is approximately given by,

$$\frac{B_g(l_g)}{B_{g0}} \approx \frac{l'_{mc} + l_{g0}}{l'_{mc} + l_g} = \frac{l'_{mc}/l_{g0} + 1}{l'_{mc}/l_{g0} + l_g/l_{g0}} \tag{3}$$

The equation is exact for (2) but is an approximation for (1) where it is assumed that $l_m/\mu_{rm} \gg l_c/\mu_{rc}$ which is generally true as in PM machines the magnet thickness and permeability of the iron core are both normally large.

The second part of (3) is obtained by dividing both the numerator and denominator by the nominal airgap l_{g0} to give a useful normalised relationship for B_g/B_{g0} as a function of the normalised airgap l_g/l_{g0} with the parameter l'_{mc}/l_{g0}. The term l'_{mc} can be interpreted as the equivalent magnetic length of air for the magnet and core material, and so l'_{mc}/l_{g0} is the normalised value of this.

Soft magnetic materials saturate at high values of magnetic flux density. In this work the core material is assumed to have relative permeability μ_{rc} until it saturates at B_{sat}. Hence from (3),

$$\frac{B_g(l_g)}{B_{g0}} = \min\left(\frac{B_{sat}}{B_{g0}}, \frac{l'_{mc}/l_{g0} + 1}{l'_{mc}/l_{g0} + l_g/l_{g0}}\right) \tag{4}$$

For PM machines, if the magnet thickness l_m is large relative to the nominal airgap l_{g0} and the magnet relative permeability is low, $\mu_{rm} \approx 1$, then l'_{mc}/l_{g0} becomes large and thus $B_g/B_{g0} \approx 1$ and thus the flux density is relatively insensitive to airgap. For PM machines with slotless stators, the magnet thickness becomes more comparable to the nominal airgap length, i.e. $l'_{mc}/l_{g0} \approx 1$. On the other hand for machines

without permanent magnets, such as induction machines, if the iron permeability is assumed high then $B_g/B_{g0} \propto l_{g0}/l_g$. Thus the airgap flux density B_g is inversely proportional to the airgap length l_g and only limited by saturation.

The axial force F for a single-sided axial-flux machine of airgap surface area A operating with an airgap flux density B_g is given by,

$$F(l_g) = \frac{1}{2}\frac{[B_g(l_g)]^2}{\mu_0}A \tag{5}$$

The airgap surface area A can be expressed as a function of the axial-flux machine's outer diameter D_o and inner diameter D_i as,

$$A = \frac{\pi(D_o - D_i)^2}{4} \tag{6}$$

It should be noted that to a first approximation the axial force is independent of the number of poles or slots.

Now defining the force F_{g0} as the force from (5), associated with the flux density B_{g0} obtained with the nominal gap l_{g0} from (1) or (2), then,

$$\frac{F(l_g)}{F_{g0}} = \left[\min\left(\frac{B_{sat}}{B_{g0}}, \frac{l'_{mc}/l_{g0}+1}{l'_{mc}/l_{g0}+l_g/l_{g0}}\right)\right]^2 \tag{7}$$

Ignoring saturation, the (negative) stiffness in the axial direction can be found as,

$$\frac{dF}{dl_g} = \frac{AB_g}{\mu_o}\frac{dB_g}{dl_g} \tag{8}$$

This can be normalised to a base stiffness which is arbitrarily chosen as the force changing from F_{g0} to zero over a distance of l_g,

$$\frac{dF/dl_g}{F_{g0}/l_{g0}} = \frac{A}{\mu_o}\frac{B_g}{B_{g0}}\frac{dB_g}{dl_g} \tag{9}$$

Fig. 3 shows plots of normalised flux density B_g/B_{g0} and axial force $F(l_g)/F_{g0}$ versus l_g/l_{g0} for three values of $l'_{mc}/l_{g0} = \infty$, 1 and 0 based on (4) and (7) for values of $B_{sat}/B_{g0} = 1.2$, 1.5 and ∞. For large values of l'_{mc}/l_{g0} (e.g. PM machines) there is a small variation of force with airgap. As this value reduces $l'_{mc}/l_{g0} = 1$ or 0 (e.g. IM), the variation increases substantially. The effect of the factor B_{sat}/B_{g0} is to limit the maximum value of flux density and hence force.

With regards to the negative stiffness, this is given by the rate of change of force with airgap. It is clear from Fig. 3 that for finite values of l_g/l_{g0}, the negative stiffness increases significantly at small values of airgap.

B. Analytical Force Model - Voltage-Driven Case

The above analysis applies for the PM-excited core or for when the electrically-excited actuator is current-driven, that is, it is assumed that the excitation is fixed. For the voltage-driven case, it is assumed that a voltage source is applied to the coil. This case models examples like mains-operated induction machines.

In the standard induction machine equivalent circuit, under no-load conditions and ignoring the stator winding and core

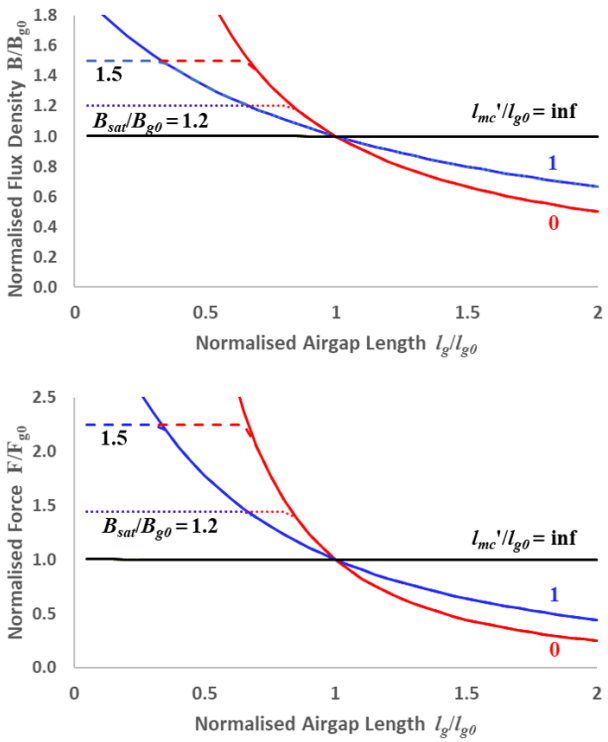

Fig. 3. Case 1: Axial-flux PM and current-excited axial-flux IMs: variation of normalised flux density (upper) and axial force (lower) versus normalised airgap for different values of normalised effective magnet and core magnetic length l'_{mc}/l_{g0} and saturation flux density B_{sat}/B_{g0}.

loss resistances, the machine can be represented by a series combination of the stator leakage inductance L_{ls} and the magnetising inductance L_m. The induced voltage is the voltage across the magnetising inductance, and is proportional to the airgap magnetic flux.

To a first approximation, the stator leakage inductance is not affected by variation of the airgap, but the magnetising inductance is given by,

$$L_m(l_g) = \frac{N^2}{R} = N^2\left[\frac{l_c}{\mu_{rc}\mu_0 A} + \frac{l_g}{\mu_0 A}\right]^{-1} = \frac{\mu_0 A N^2}{(l'_c + l_g)} \tag{10}$$

where $l'_c = l_c/\mu_{rc}$. For an applied frequency f_s, the electrical angular frequency is $\omega_e = 2\pi f_s$. For a given applied supply phase voltage V_s, the resultant (no-load) current I will then be,

$$I(l_g) = \frac{V_s}{\omega_e(L_m + L_{sl})} = \frac{V_s}{\omega_e[\mu_0 A N^2/(l'_c + l_g) + L_{sl}]} \tag{11}$$

The ratio of the no-load stator current I with an airgap l_g to the stator current I_{g0} with the nominal airgap l_{g0} is,

$$\frac{I(l_g)}{I_{g0}} = \frac{\mu_0 A N^2/(l'_c + l_{g0}) + L_{sl}}{\mu_0 A N^2/(l'_c + l_g) + L_{sl}} \tag{12}$$

From this equation, the ratio I_g/I_{g0} can be plotted as a function of the ratio l_g/l_{g0} with two parameters: the normalised effective magnetic core length l'_c/l_{g0} and the ratio

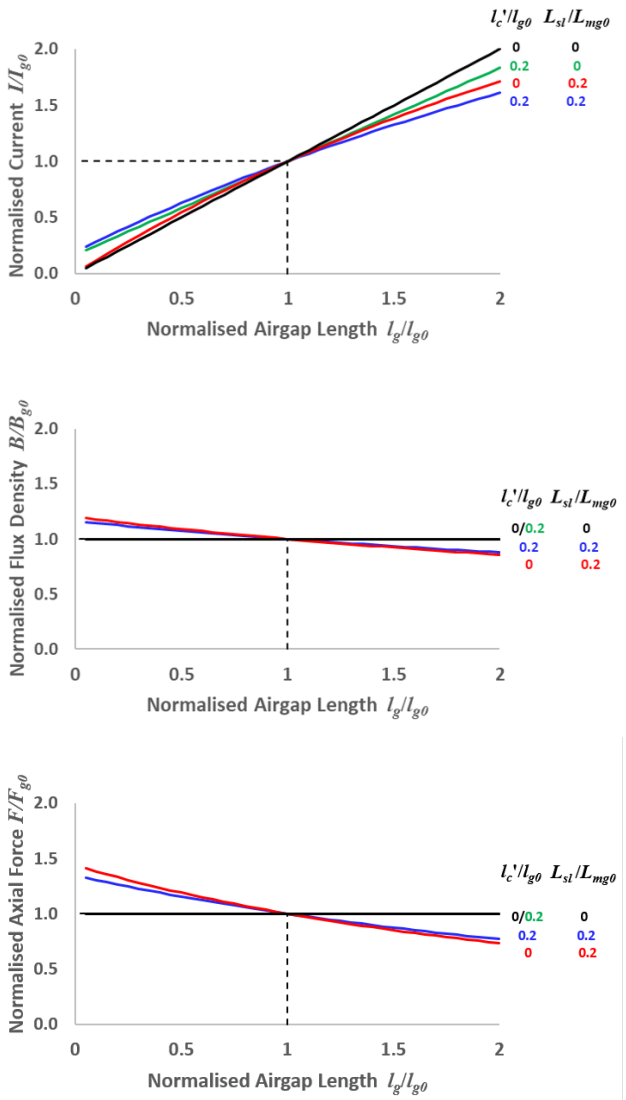

Fig. 4. Case 2: Voltage-driven axial-flux IMs: analytical current (upper), flux density (middle) and axial force (lower) vs airgap for l_c'/l_{g0} = 0 and 0.2 and for L_{ls}/L_{mg0} = 0 and 0.2

of the leakage inductance to the magnetising inductance with nominal gap L_{sl}/L_{m0}. This is shown in the upper graph in Fig. 4. It can be seen that with voltage excitation the (no-load) current is roughly linearly proportional to the airgap length. This is reasonable as voltage excitation is effectively near constant flux operation and hence the current is proportional to the circuit reluctance.

The largest variation in current with airgap occurs with the two parameters equal to zero. Adding finite core permeability means that with zero airgap, there is still a finite magnetising current. Adding the leakage inductance reduces the magnetising current at higher airgaps.

It should be noted that ignoring the leakage inductance L_{sl}, the current ratio with $l_g = 0$ is approximately given by,

$$\frac{I(l_g = 0)}{I_{g0}} \approx \frac{l_c'/l_{g0}}{l_c'/l_{g0} + 1} \tag{13}$$

The induced voltage E across the magnetising inductance is proportional to the flux-linkage and hence airgap flux density. This induced voltage is given by,

$$E(l_g) = V\frac{\omega L_m}{\omega(L_m + L_{sl})} = V\frac{1}{1 + L_{sl}/L_m} \tag{14}$$

Thus the ratio of the induced voltage E to the induced voltage E_{g0} with the nominal airgap is given by,

$$\frac{E(l_g)}{E_{g0}} = \frac{L_{mg0} + L_{sl}}{L_m + L_{sl}} = \frac{\mu_0 N^2 A + L_{sl}(l_c' + l_{g0})}{\mu_0 N^2 A + L_{sl}(l_c' + l_g)} \tag{15}$$

This is the same relationship as between $B(l_g)/B_{g0}$.

The middle graph in Fig. 4 shows the variation of normalised flux density B/B_{g0} versus normalised airgap length l_g/l_{g0}. For this voltage-driven case, the flux density is not affected by finite core permeability and hence the black and green curves overlap and are horizontal lines. Thus the flux density is only significantly affected by the leakage inductance in this case.

The lower graph shows the variation of normalised axial force which is basically the square of the normalised flux density variation shown in the middle graph. It shows that for voltage-driven axial-flux IMs, the key parameter affecting the variation of axial force with airgap is the ratio of the stator leakage inductance to the magnetising inductance L_{ls}/L_{mg0} and that the normalised effective magnetic core length l_c'/l_{g0} has little effect.

III. Axial-Flux PM Machine Case Study

Table I shows the design parameters of the axial-flux PM machine used as a case study for the comparison of the analytical and 3D FE unbalanced axial force analysis.

This PM machine has an airgap of 2 mm. The magnets and core material add an additional 5.65 mm of effective airgap (see Table I) to create a total effective airgap of 7.64 mm.

In an axial-flux PM machine, the stator teeth only cover a fraction of the airgap surface. The ratio of stator teeth area to total airgap area is given by α. In addition, the ratio of the magnet area to the total airgap area is given by β. The peak flux density $B_g(l_g)$ is still given by (1) but the average airgap flux density B_{g-avg} will be roughly given by,

$$B_{g-avg}(l_g) \approx \alpha\beta B_g(l_g) \tag{16}$$

The total force will be given by modifying (5) to include the stator teeth and magnet area ratios,

$$F_{avg}(l_g) \approx \alpha\beta F(l_g) \tag{17}$$

A 3D FE model of the machine was created and the airgap flux density distribution was found. The axial force was found using two methods. Firstly, by finding the average airgap flux

TABLE I
AXIAL-FLUX PERMANENT MAGNET MACHINE PARAMETERS

Parameter	Value
Rated power	35 kW
Rated speed	2,000 rpm
Poles	12
Outer diameter	400 mm
Inner diameter	280 mm
Stator teeth airgap area to total airgap area α	79%
Airgap length l_{g0}	2 mm
Magnet remanent flux density B_r	1.079 T
Magnet pole area to total airgap area β	70%
Magnet thickness l_m	6 mm
Magnet relative permeability μ_{rm}	1.07
Effective magnet thickness l'_m	5.61 mm
Core mean half magnetic path length l_c	112 mm
Core unsaturated relative permeability μ_{rc}	4,300
Effective half core unsaturated length l'_c	0.026 mm
Effective magnet and half core length l'_{mc}	5.64 mm

density and then using (5) based on average airgap flux density and the total airgap area. Secondly, by applying (5) on point-by-point basis on the rotor and integrating the result to find the total force on the rotor. The latter is equivalent to finding the rms flux density value. This technique will give a larger and more accurate value given the square law relationship between force and flux density.

The results from the analysis of the axial-flux PM machines are shown in Fig. 5. The upper figure shows a comparison of the average airgap flux density calculated from FEA versus the analytical result from (16) showing a good match. The lower figure shows three curves for axial force versus airgap. The solid blue line is based on the average airgap flux density from FEA while the solid red line is based on the rms airgap flux density from FEA which is significantly higher as expected. The dashed red line is the simple analytical approximation. The analtyical result significantly over predicts the force but does show a similar trend to the FEA results. The analytical approximation effectively assumes a square-wave airgap flux distribution with constant flux when magnets and stator teeth coincide and zero flux elsewhere. In practice the airgap flux distribution is more complex than this, which results in a smaller difference between the average and rms values compared to a square wave.

IV. AXIAL-FLUX INDUCTION MACHINE CASE STUDY

Table II shows the design parameters of the axial-flux induction machine used for the voltage and current-driven analysis. It should be noted that the effective magnetic airgap of this machine (0.502 mm) is an order of magnitude smaller than for the axial-flux PM machine (7.64 mm).

A. Voltage-Driven Axial-Flux Induction Machine

3D FEA was used to obtain the current, flux density and axial force versus airgap for the voltage-driven axial-flux IM as shown as red squares in Fig. 6 along with the analytical predictions shown as blue dashed lines.

The upper figure shows the (no-load) current which has the expected nearly linear relationship with airgap length seen

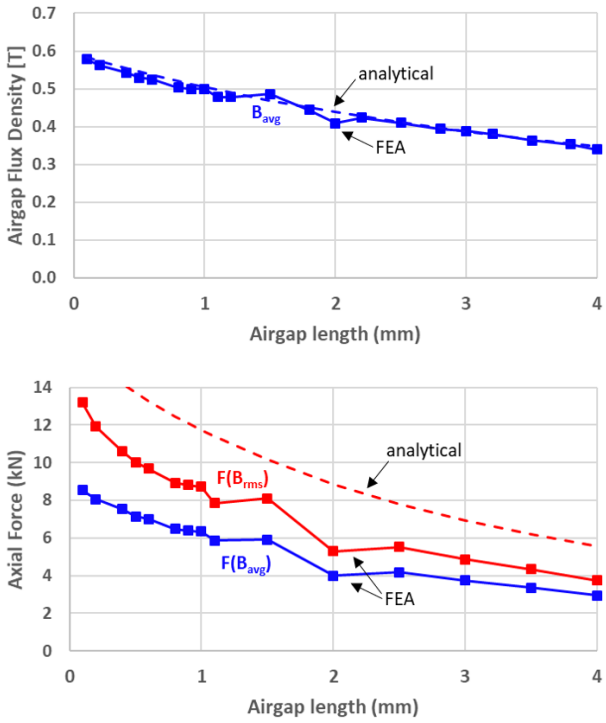

Fig. 5. Axial-flux PM machine: comparison of analytical and FE calculated average flux density and force versus airgap.

TABLE II
AXIAL-FLUX INDUCTION MACHINE PARAMETERS

Parameter	Value
Rated power	2.2 kW
Rated frequency	50 Hz
Rated speed	727 rpm
Poles	8 poles
Outer diameter	280 mm
Inner diameter	163 mm
Airgap length l_{go}	0.5 mm
Core mean half magnetic path length l_c	84 mm
Core unsaturated relative permeability μ_{rc}	5,000
Effective half core unsaturated length l'_c	0.017 mm
Ratio of l'_c/l_{g0}	0.034
Stator leakage inductance L_{sl}	17.2 mH
Magnetising inductance L_m	234 mH
Ratio of L_{sl}/L_m	0.0735

earlier in Fig. 4. Based on the extrapolated 3D FEA results, at zero airgap the no-load current is about 1.2 A compared to the value of about 3.2 A with nominal airgap. Thus based on (13), this gives a value of $l'_c/l_{g0} \approx 0.6$. This value is about an order of magnitude larger than the calculated value based on the core magnetic path length and the unsaturated relative permeability shown in Table II of 0.0735, and this is likely due to a significant degree of magnetic saturation under no-load conditions.

It should be noted that based on Fig. 4 it can be seen that while the parameter l'_c/l_{g0} has a significant effect on the current versus airgap characteristic, it has little effect on the flux density and force versus airgap curves. For these the

parameter L_{sl}/L_{mg0} is the critical factor. Locked-rotor and no-load simulations were performed using FEA and the results are given in Table II and show a value of L_{sl}/L_{mg0} of 0.0735. It was assumed that the stator and rotor leakage inductances are equal.

The upper graph of Fig. 6 shows that using the curve-fitted value of $l'_c/l_{g0} \approx 0.6$, the FEA calculated value of $L_{sl}/L_{mg0} = 0.0735$ and the FEA calculated value at nominal airgap, gives an analytical prediction (dashed blue lines) which match the FEA results (red squares) fairly well. The middle graph shows the airgap flux density and lower graph shows the axial force. For both these graphs the analytical prediction was used to predict only the variation and thus used the corresponding FEA calculated value at the nominal airgap as the reference point. Based on this, it was found that the analytical prediction (blue dashed lines) matched the trends in the FEA results (red squares) well.

V. Conclusions

This paper has used a simplified analytical model to show that the variation of axial force with airgap length in axial-flux machines depends on whether the machine is a permanent magnet (PM) machine or else a current or voltage-driven induction machine (IM).

For PM machines and current-driven IMs, it is dependent on the effective total magnet and core magnetic length, where the larger this value, the lower the force variation with airgap. As axial-flux PM machines have magnets which are generally thick compared to the airgap, this means these have smaller force variations with airgap than current-driven axial-flux IMs. The force is also limited by the saturation flux density.

For voltage-driven axial-flux IMs, while the current versus airgap is most sensitive to the ratio of the effective core magnetic length to airgap length, the flux density and axial force are most sensitive to the ratio of the leakage inductance to the magnetising inductance, where the lower the leakage inductance, the smaller the force variation with airgap.

In the proposed future work, the above results will be validated using experimental results on a prototype machine.

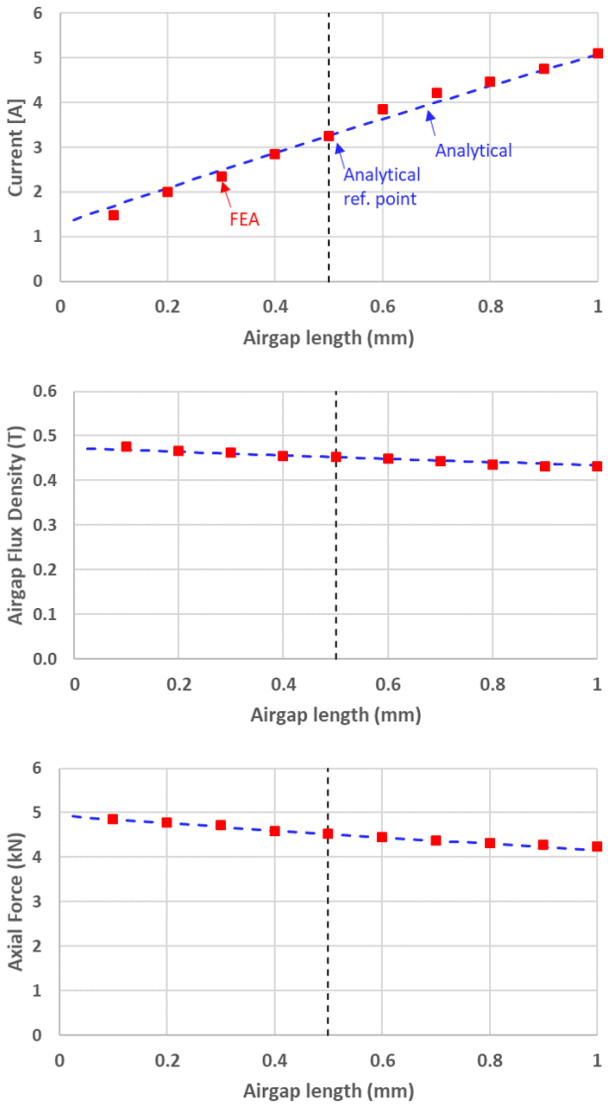

Fig. 6. Voltage-driven axial-flux induction machine: FEA and analytically calculated current, magnetic flux density and force versus airgap. The analytical calculations were done with l'_c/l_{g0} = 0.6 and L_{sl}/L_{mg0} of 0.0735 and used the FEA values at the nominal airgap as a reference point.

References

[1] O. Bouaziz, I. Jaafar, and F. Ben Ammar, "Performance analysis of radial and axial flux PMSM based on 3D FEM modeling," *Turkish Journal of Electrical Engineering & Computer Sciences*, vol. 26, pp. 1587–1598, 2018.

[2] X. Zhang and B. Zhang, "Analysis of magnetic forces in axial-flux permanent-magnet motors with rotor eccentricity," *Hindawi Mathematical Problems in Engineering*, vol. 2021, 2021.

[3] B. Guo, Y. Du, F. Peng, and Y. Huang, "Magnetic field calculation in axial flux permanent magnet motor with rotor eccentricity," *IEEE Transactions on Magnetics*, pp. 1–1, 2022.

[4] P. Jin, Y. Yuan, J. Minyi, F. Shuhua, L. Heyun, H. Yang, and S. L. Ho, "3-D analytical magnetic field analysis of axial flux permanent-magnet machine," *IEEE Transactions on Magnetics*, vol. 50, no. 11, pp. 1–4, 2014.

[5] Q. Wang, F. Zhao, and K. Yang, "Analysis and optimization of the axial electromagnetic force for an axial-flux permanent magnet vernier machine," *IEEE Transactions on Magnetics*, vol. 57, no. 2, pp. 1–5, 2021.

[6] S. M. Mirimani, A. Vahedi, and F. Marignetti, "Effect of inclined static eccentricity fault in single stator-single rotor axial flux permanent magnet machines," *IEEE Transactions on Magnetics*, vol. 48, no. 1, pp. 143–149, 2012.

[7] A. Parviainen, M. Niemela, and J. Pyrhonen, "Modeling of axial flux permanent-magnet machines," *IEEE Transactions on Industry Applications*, vol. 40, no. 5, pp. 1333–1340, 2004.

[8] J. Li, R. Qu, and Y.-H. Cho, "Effect of unbalanced and inclined air-gap in double-stator inner-rotor axial flux permanent magnet machine," in *2014 International Conference on Electrical Machines (ICEM)*, 2014, pp. 502–508.

[9] W. Tong, S. Wang, S. Dai, S. Wu, and R. Tang, "A quasi-three-dimensional magnetic equivalent circuit model of a double-sided axial flux permanent magnet machine considering local saturation," *IEEE Transactions on Energy Conversion*, vol. 33, no. 4, pp. 2163–2173, 2018.

[10] Z. Nasiri-Gheidari and H. Lesani, "New design solution for static eccentricity in single stator–single rotor axial flux induction motors," *IET Electric Power Applications*, vol. 7, pp. 523–534, 2013.